

# Numerical assessment of the new V-shape small-angle slot divertor on DIII-D

R. Maurizio,<sup>1,2</sup> H. Du,<sup>3</sup> A. Gallo,<sup>1</sup> H. Guo,<sup>2</sup> A. Leonard,<sup>2</sup> X. Ma,<sup>1</sup> G. Sinclair,<sup>2</sup> P. Stangeby,<sup>4</sup> D. Thomas,<sup>2</sup> H. Wang,<sup>2</sup> R.S. Wilcox,<sup>5</sup> J.H. Yu,<sup>2</sup> L. Casali,<sup>2</sup> and M.W. Shafer<sup>5</sup>

<sup>1)</sup>Oak Ridge Associated Universities, Oak Ridge, 37830 TN, USA

<sup>2)</sup>General Atomics, San Diego, 92186 CA, USA

<sup>3)</sup>Southwestern Institute of Physics, Chengdu 610041, People's Republic of China

<sup>4)</sup>University of Toronto, Toronto, ON, M3H 5T6 Canada

<sup>5)</sup>Oak Ridge National Laboratory, Oak Ridge, 37831 TN, USA

(Dated: 6 July 2021)

**Abstract** The small-angle slot (SAS) divertor of the DIII-D tokamak, and its upcoming upgrade, the V-shape small-angle slot (SAS-V) divertor, are numerically investigated using the SOLPS-ITER code package, including the effect of particle drifts, for a range of plasma density, heating power, strike point position in the slot, and for both magnetic field directions. The simulations show that the electron temperature near the strike point is reduced in SAS-V compared to SAS, for both magnetic field directions, such that SAS-V achieves divertor detachment at a lower value of the outboard mid-plane separatrix electron density. The detachment threshold is lower because the V-shape focuses recycling neutrals on the V-end, densifying and cooling the plasma in the slot. At sufficiently high density, the V-shape also reduces the radial gradient of the temperature profile at the target, which in turns reduces the radial electric field and the  $\mathbf{E} \times \mathbf{B}$  drift velocities, further densifying and cooling the plasma in the slot and leading to detachment. The V-shape effect, however, is reduced for higher heating power. With more heating power, the detachment density increases, reducing the ionization mean free path of recycled neutrals, which therefore become less sensitive to target shape changes. This suggests that in a fusion reactor, where the heating power is high, optimization of the divertor target shape needs to be combined with other strategies to lower the detachment density, such as in-slot injection of low-Z impurities.

## I. INTRODUCTION

A critical open challenge for the design and operation of a future nuclear fusion reactor is the management of the plasma exhaust power, which continually flows out of the confined plasma towards the divertor targets. Safe and durable operation of a reactor imposes, at the divertor targets, unmitigated peak heat load  $\leq 10\text{-}15 \text{ MW/m}^2$  and electron temperature  $\leq 5\text{-}10 \text{ eV}$  [1,2]. Accurate design of the divertor target shape can maximize the density of recycled neutrals near the target, thus enhancing volumetric energy dissipation and ionization, which lower both heat load and electron temperature. Divertor shape optimization, through experiments and numerical modeling, has been a fruitful research area for decades [3–10].

Recently, a Small-Angle Slot (SAS) divertor concept has been installed and tested on the DIII-D tokamak [11]. This concept was designed using the two-dimensional boundary package SOLPS 5.0-EIRENE without including particle cross-field drifts [12]. The design aimed at enhancing neutral trapping inside the slot and thus increasing plasma cooling along the target. Experimental tests on DIII-D find that the target electron temperature is lower in SAS relative to a matched open divertor configuration, thus lowering the outboard mid-plane separatrix electron density required to detach the divertor. However, these benefits are only observed for the ion  $\mathbf{B} \times \nabla \mathbf{B}$  out of the divertor, and are much smaller for the opposite field direction. More recently, a modified version of the SAS concept has been proposed and will be tested on DIII-D. This new concept was designed using the two-dimensional boundary package SOLPS-ITER, in-

cluding  $\mathbf{E} \times \mathbf{B}$  particle drifts [13]. The upgraded version of SAS features a V-shape slot end instead of a flat end and so is named "SAS-V". Modeling indicated that SAS-V reduced target electron temperature relative to SAS in a similar way for both field directions. Consequently, SAS-V should achieve lower target temperatures than a matched open divertor configuration for both field directions. The first modeling effort of SAS-V used a set of simplifications to facilitate convergence and accelerate the modeling process. For instance, it used a simplified SAS and SAS-V geometry, relative to that employed in DIII-D, lower input power that normally used for testing SAS in DIII-D, and did not include the effect of diamagnetic or viscosity drifts.

This paper presents SOLPS-ITER modeling of SAS and SAS-V without many of the approximations that were used in the first modeling of SAS-V. Also, to further increase accuracy, data collected in previous SAS experiments is used to determine realistic modeling inputs. For instance, the cross-field anomalous transport coefficients are estimated using electron density and temperature measurements around the plasma. Modeling of SAS and SAS-V is done for a range of plasma densities, input powers, strike point positions, and for both magnetic field directions.

This set of simulations not only assesses the performance of the SAS-V divertor compared to SAS, but also thoroughly investigates the impact of divertor closure and particle drifts on detachment. The results will guide the upcoming SAS-V experimental test on DIII-D, and highlight key divertor physics and design parameters for the design and operation of a new DIII-D upper divertor.

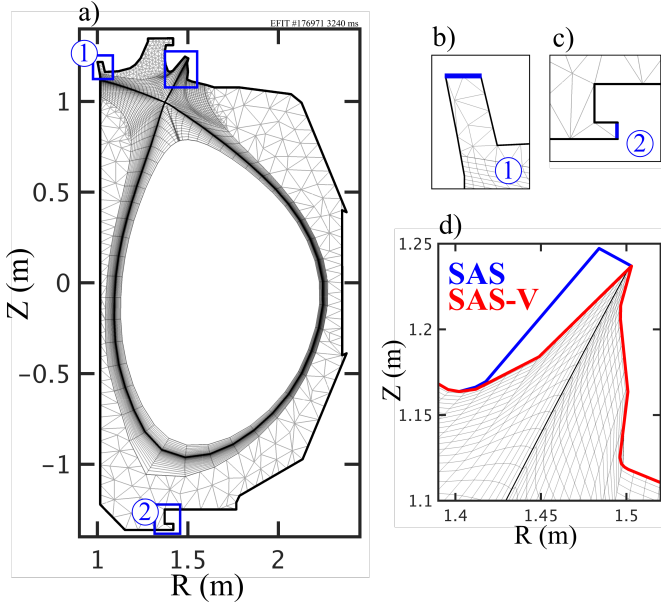


FIG. 1. SOLPS-ITER computational mesh (a), with a details of the upper inner (b) and lower (c) cryopumps. (d) Details of the mesh in the slot, for the existing SAS divertor (blue) and the planned SAS-V divertor (red).

The paper is organized as follows. Section II describes the set of inputs to the simulations, including the conditions at the computational grid boundary (section II A) and the cross-field anomalous transport coefficients (section II B). The performance of SAS and SAS-V is assessed by scanning the plasma density, section III, for both magnetic field directions. The effect of the heating power is discussed in section III C. Then, performance is further evaluated by sweeping the strike point across each slot at fixed plasma density, section IV. Finally, a summary and some conclusions are discussed in section V.

## II. MODELING SETUP

The modeling is performed using the SOLPS-ITER code package [14] (version 3.0.6), which couples the 2D multi-fluid plasma transport code B2.5 [15] and the 3D kinetic neutral transport code EIRENE [16]. B2.5 provides the plasma background to EIRENE, which computes and returns the source and sink terms for plasma particles, momentum and energy due to plasma-neutral collisions. Modeling is carried out for a deuterium plasma with carbon wall and targets. The plasma species are  $D^+$ ,  $C^+$  ...  $C^{6+}$  and the neutral species are D,  $D_2$  and C. A wide range of reactions is included by EIRENE (Table I). Simulations include neutral-neutral collisions, all particle drifts ( $\mathbf{E} \times \mathbf{B}$ ,  $\mathbf{B} \times \nabla \mathbf{B}$ , viscosity) and the associated currents.

The computational mesh is built using the DIII-D magnetic equilibrium of shot 176971 at 3240 ms, as computed by the EFIT equilibrium reconstruction code [17], and

Database	Physical reaction
AMJUEL H.4 H.10 2.1.5	$D + e \rightarrow D^+ + 2e$
HYDHEL H.1 H.3 3.1.8	$D^+ + D \rightarrow D + D^+$
AMJUEL H.4 H.10 2.6A0	$C + e \rightarrow C^+ + 2e$
METHAN H.1 H.3 3.2	$D^+ + C \rightarrow D + C^+$
AMJUEL H.4 2.2.9	$D_2 + e \rightarrow D_2^+ + 2e$
AMJUEL H.4 2.2.5g	$D_2 + e \rightarrow D + D + e$
AMJUEL H.4 2.2.10	$D_2 + e \rightarrow D + D^+ + 2e$
AMJUEL H.0 H.1 H.3 0.3T	$D_2 + D^+ \rightarrow D_2 + D^+$
AMJUEL H.2 3.2.3	$D_2 + D^+ \rightarrow D_2^+ + D$
AMJUEL H.4 2.2.12	$D_2^+ + e \rightarrow D + D^+ + e$
AMJUEL H.4 2.2.11	$D_2^+ + e \rightarrow D^+ + D^+ + 2e$
AMJUEL H.4 H.8 2.2.14	$D_2^+ + e \rightarrow D + D$
AMJUEL H.4 H10 2.1.8	$D^+ + e \rightarrow D$
AMJUEL H.4 H10 2.1.8	$D^+ + 2e \rightarrow D + e$
ADAS H.4 acd96/H.10 prb96	$C^+ + e \rightarrow C + h\nu$
CONST H.2	$D + D \rightarrow D + D$
CONST H.2	$D_2 + D_2 \rightarrow D_2 + D_2$
CONST H.2	$D + D_2 \rightarrow D + D_2$
CONST H.2	$D_2 + D \rightarrow D_2 + D$

TABLE I. Physical reactions between neutrals and plasma particles, included in EIRENE.

is shown in figure 1. This shot has plasma current of 1 MA, toroidal magnetic field at the magnetic axis of  $B_t = 2$  T, ion  $\mathbf{B} \times \nabla \mathbf{B}$  drift into the divertor, total input power of  $P_{\text{tot}} = 4.55$  MW (from auxiliary and Ohmic heating) and core radiation of  $P_{\text{rad,core}} = 0.4$  MW. To model the opposite ion  $\mathbf{B} \times \nabla \mathbf{B}$  drift direction (out of the divertor), plasma shot 176310 at 2960 ms is selected, as it matches the magnetic equilibrium and global properties of shot 176971 (plasma current, toroidal field, heating power, core radiation, line-averaged electron density). Since the magnetic equilibrium is the same for both reference plasma shots, only one mesh is used to model both drift directions. The plasma grid has a resolution of 95 x 40 cells in the poloidal x radial directions. It extends from  $R - R_{\text{sep}} = -1$  cm to  $R - R_{\text{sep}} = 2.5$  cm, where  $R - R_{\text{sep}}$  is the radial distance from the separatrix at the plasma outboard mid-plane, corresponding to  $\psi_n \approx 0.95$  to 1.07. The cryopump located at the top inner corner and that located below the bottom shelf are modeled as surfaces that absorb 30% of the impinging particle flux, with no distinction between neutrals and ions, see figure 1b-c.

Two slot configurations are modeled, the existing Small-Angle Slot (SAS) divertor and a modified version of SAS, featuring a V-corner and thus named SAS-V, which will be installed and tested. The V-shape is obtained by modifying the inboard side of the slot, as shown in figure 1d, connecting, in the poloidal plane, the slot entrance inner corner to the flat end outer corner. An intermediate point is added to the newly created slant, to further reduce the V-corner angle to  $\approx 30^\circ$ . A smaller

angle is not chosen because it would drastically reduce our ability to diagnose the plasma in the slot.

### A. Boundary conditions

At the core boundary of the grid, the plasma power flux is evenly split between electrons and ions, and set to  $P_{\text{SOL}} = 4$  MW, to match the power crossing the separatrix for the reference shot,  $P_{\text{SOL}} \approx P_{\text{tot}} - P_{\text{rad,core}}$ . The average value of the ion density along the inner boundary is set to a fixed value, which is changed from case to case to model the evolution of the divertor from attached to detached regime. At the outer boundary of the grid in the Common Flux Region (CFR), a leakage flux is set for the electron energy, the ion energy and the ion density. The electron and ion energy leakage fluxes are set to 0.1% and 1% of the sound-speed energy flux, respectively. The ion density flux is set to 0.2% of the ion sound-speed flux. At the outer boundary of the grid in the Private Flux Region (PFR), the electron and ion energy leakage fluxes are set to 0.01% and 1% of the sound-speed energy flux respectively, the ion density leakage rate to 0.1% of the ion sound speed flux. The leakage flux magnitude is similar to recent SOLPS-ITER modeling of DIII-D plasmas [18]. The plasma flux leaving the grid across the last radial grid surface is recycled as neutrals. At the targets, recycling is set to 100% with standard pre-sheath boundary conditions. At the first-wall surface, recycling is set to 99%. Sputtering of carbon is implemented for all wall elements except the cryopumps. Physical sputtering uses the Roth-Bohdansky model [19], chemical sputtering from incoming D and D+ uses a fixed 2% yield.

### B. Anomalous transport coefficients

The cross-field anomalous transport coefficients for the main SOL (i.e. around the confined plasma) are determined by matching the outboard mid-plane electron temperature and density profiles from the simulation with those measured experimentally using a Thomson Scattering system. This is done iteratively until a satisfactory match is achieved, as described in [20]. Particle diffusivity  $D$  and electron thermal diffusivity  $\chi_e$  are estimated using the measured profiles of electron density and temperature, respectively. Ion thermal diffusivity  $\chi_i$ , however, cannot be determined using the same procedure due to lack of good ion density measurements in the SOL, and is therefore set equal to  $\chi_e$ . In the divertor (between target and X-point), the transport coefficients are set spatially constant, with  $D=0.3$  m<sup>2</sup>/s and  $\chi_e = \chi_i = 1$  m<sup>2</sup>/s. These values are chosen because they match the main SOL transport coefficients at the separatrix, as shown in the next paragraph.

The procedure is done for the reference plasma shot with ion  $\mathbf{B} \times \nabla \mathbf{B}$  drift into the divertor (shot 176310). The ion density at the inner boundary (IB) of the grid,

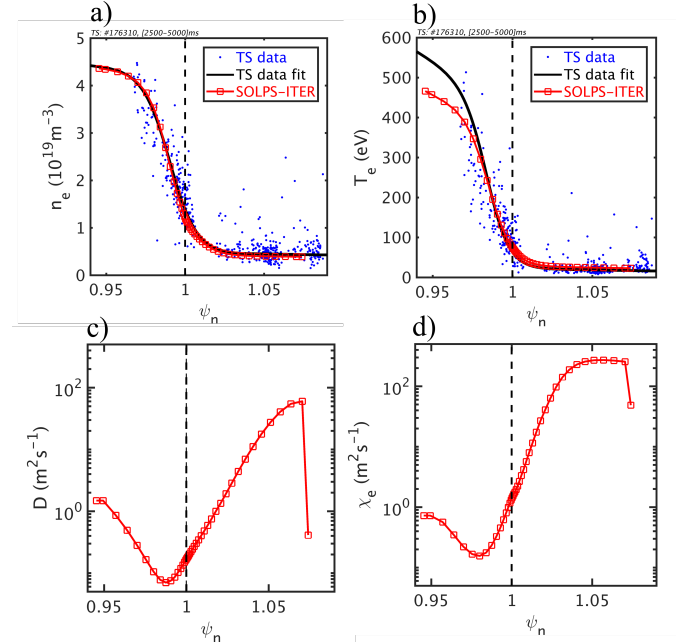


FIG. 2. Outboard mid-plane electron density (a) and temperature (b) measurements from Thomson scattering (blue) for the reference shot, fitted by a modified hyperbolic function (black), compared to those of the SOLPS-ITER run. (c-d) Cross-field anomalous transport coefficients of the SOLPS run, determined by the fitting procedure.

located at  $\psi_n = 0.945$ , is set to  $n_{e,\text{IB}} = 4.2 \cdot 10^{19} \text{ m}^{-3}$  to match the experimentally measured electron density at that location  $n_{e,\text{IB}} \approx 4.4 \cdot 10^{19} \text{ m}^{-3}$ . The experimental profiles used for the matching are modified hyperbolic tangent fits to the measured data point, see figure 2 a-b.

After a few iterations, the fitting procedure yields a general good match in the outer mid-plane profiles of electron density and temperature between measurements and modeling, figure 2a-b, except for the electron temperature near the grid inner boundary. The profile shape for particle and electron heat diffusivity are similar, with a minimum inside the separatrix, followed by a rapid and steady increase in the SOL, figure 2c-d. Such a strong radial transport in the far-SOL reflects the relatively high electron density and temperature measured by TS ( $\approx 17$  eV and  $0.4 \cdot 10^{19} \text{ m}^{-3}$  at  $\psi_n=1.07$ ). The transport coefficients at the separatrix roughly match the values prescribed in the divertor. No effect on the simulated solution is observed if the transport profiles determined by the fitting procedure are extended to the divertor SOL.

Good agreement between modeling and measurements is also achieved at the outer target. Figure 3 shows the electron density and temperature, measured with a Langmuir Probe array, and the incoming neutral deuterium flux, derived from two in-tile pressure gauges (labeled SAS1A and SAS1B) [21]. The incoming neutral deuterium flux (atomic and molecular) is computed from the measured molecular deuterium pressure  $P_{D2}$  with  $\Gamma_{D, D2}^{\text{inc}} = P_{D2} \sqrt{2 / (\pi m_{D2} k_B T_{\text{wall}})}$ , where  $m_{D2}$  is the

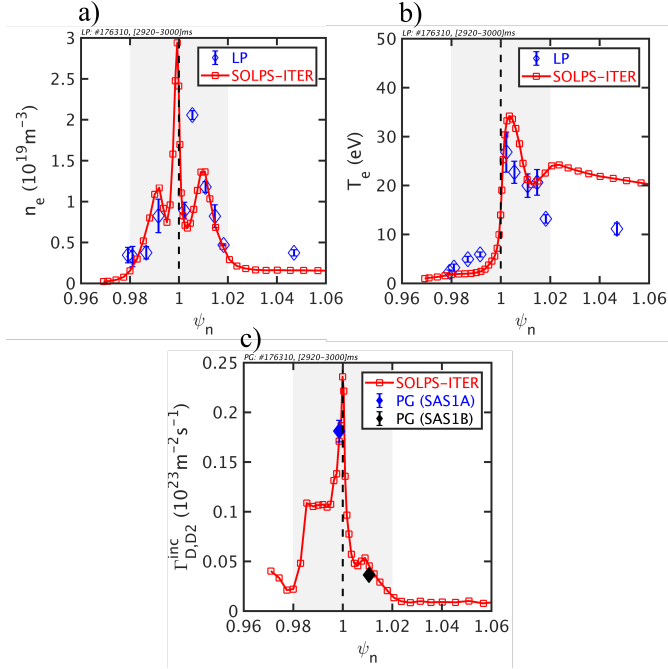


FIG. 3. Outer target electron density (a), electron temperature (b) and incoming neutral deuterium flux (c) profiles from SOLPS modeling (red line) compared to experimental measurements from Langmuir Probes (LP) and Pressure Gauges (PG). The shaded area indicates the extent of the SAS slot. The neutral deuterium flux is computed from the measured neutral pressure with the relation reported in section II B.

molecular deuterium mass,  $k_B$  the Boltzmann constant and  $T_{\text{wall}} = 300 \text{ K}$  the gauge housing wall temperature [22,23]. The agreement is particularly good inside the slot, located from  $\psi_n = 0.98$  to  $1.02$  (shaded area in the plots).

Power balance analysis of the simulation results finds that the power crossing the separatrix (3.95 MW) is in majority convected, perpendicularly to flux surfaces, towards the main chamber walls (2.88 MW), such that a small amount flows, parallel to field lines, to the inner (0.15 MW) and outer (0.68 MW) divertors, see Table II. Such a strong radial heat flux is due to the high cross-field transport coefficients in the far-SOL, figures 2c-d, which in turn reflect the high electron density and temperature measured by TS. Since the code matches the experimental plasma profiles at both the outer mid-plane and outer target, the unrealistically high power to the main chamber walls is the effect of a radiation shortfall in the SOL, i.e. the SOL radiated power in the code is much less than in the experiment. This is consistent with previous studies indicating a shortfall of radiated power in 2D fluid edge codes relative to experimental measurements [24,25]. The consequences of such radiated power shortfall will be more thoroughly investigated in future simulations.

Location	Power (MW)
Separatrix	3.95
Main chamber wall	2.88
Out. div. entrance	0.68
Out. target	0.54
Out. div. radiation	0.10
In. div. entrance	0.15
In. target	0.08
In. div. radiation	0.11

TABLE II. Power balance analysis of SOLPS-ITER simulation of SAS shot 176310, with anomalous transport coefficients determined by matching TS measurements.

### III. SCAN OF PLASMA DENSITY

The performance of the SAS and SAS-V divertors is evaluated by gradually increasing the plasma density, which causes the divertor to transition from the attached to the detached regime. The plasma density is varied by changing the prescribed value of the ion density at the grid inner boundary. The strike point position is the same for SAS and SAS-V, as shown in figure 1d.

To quantify the transition from attached to detached regime, i.e. the onset of divertor detachment, we consider the electron temperature, at the target, where the parallel heat flux is maximum in attached conditions,  $T_{e,t}$ . Due to cross-field transport of heat and particles in the divertor, the parallel heat flux profile at the target typically does not peak exactly at the strike point, but somewhere nearby in the CFR. For this set of simulations, the profile peaks at the third flux ring in the CFR, corresponding to  $\psi_n = 1.001$ . The onset of divertor detachment is here defined as when this electron temperature drops below 10 eV [1]. The corresponding value of the electron density at the outboard mid-plane separatrix, denoted as  $n_{e,\text{det}}$ , is referred to as the upstream electron density required to detach the divertor.

#### A. Ion $\mathbf{B} \times \nabla \mathbf{B}$ drift into divertor

For ion  $\mathbf{B} \times \nabla \mathbf{B}$  into the divertor, SOLPS-ITER finds that at all densities the electron temperature near the strike point is reduced in SAS-V compared to SAS, figure 4a. Consequently, the plasma in SAS-V detaches at a lower outer mid-plane separatrix electron density than in SAS. Compared to SAS, SAS-V achieves  $T_{e,t} = 10 \text{ eV}$  with 11% lower upstream separatrix density, and  $T_{e,t} = 5 \text{ eV}$  with 16% lower upstream separatrix density. These results are qualitatively consistent with the first exploratory SOLPS-ITER modeling of the SAS-V concept [13], which was performed at lower input power, with a simplified SAS/SAS-V geometry and with  $\mathbf{E} \times \mathbf{B}$  drifts only.

The lower  $n_{e,\text{det}}$  in SAS-V can be explained in terms

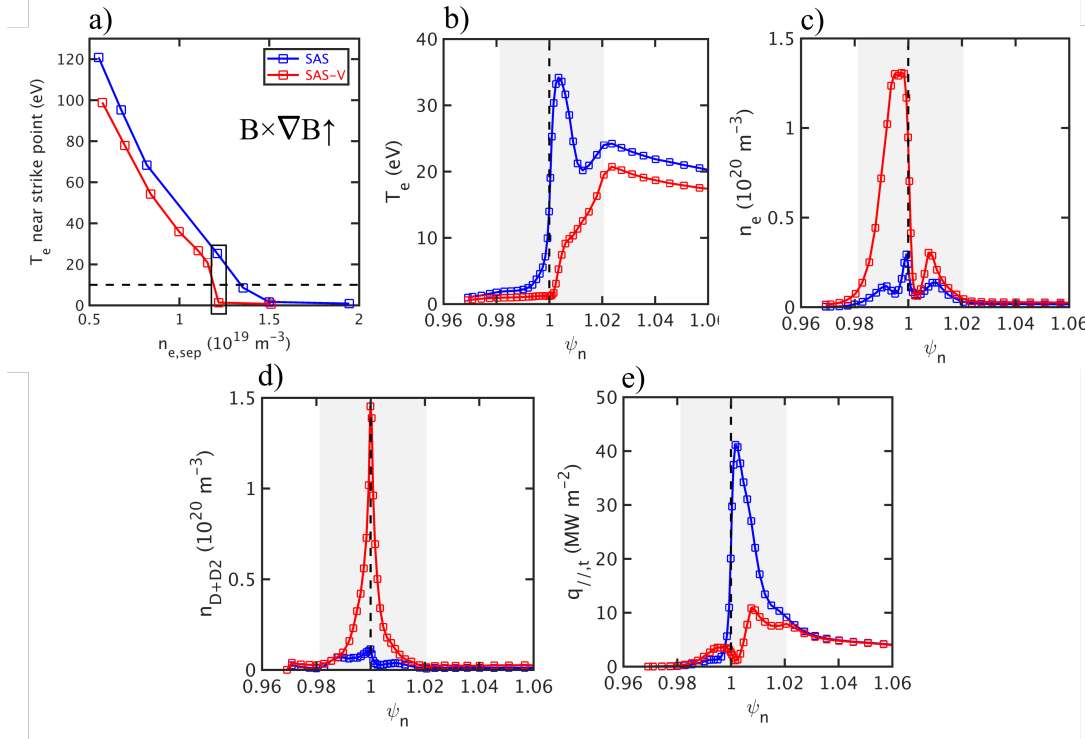


FIG. 4. For ion  $\mathbf{B} \times \nabla \mathbf{B}$  into the divertor, (a) electron temperature near the strike point (third poloidal flux ring in CFR after separatrix) as a function of the separatrix electron density at the outboard mid-plane for SAS (blue) and SAS-V (red). For the same  $B_t$  direction, at the density  $n_{e,sep} = 1.21 \cdot 10^{19} \text{ m}^{-3}$  indicated in sub-figure (a), target profiles of electron temperature (b), electron density (c), neutral density (d) and parallel heat flux (e), for SAS (blue) and SAS-V (red). The shaded area indicates the extent of the slot.

of the V-corner ability to focus neutrals. SAS-V concentrates neutrals at the V-corner, figure 4d, by directing the recycling neutrals from both common and private flux sides of the slot towards the separatrix. The higher neutral concentration increases volumetric ionization and line radiation, figures 5a-b, which densifies and cools the plasma. The cooling effect is strong enough to cause a substantial reduction of the radial gradient of  $T_e$ , figure 4b. This reduces the radial electric field and thus the  $\mathbf{E} \times \mathbf{B}$  drift velocity in the divertor, causing an additional cooling of the plasma [13]. For this  $B_t$  direction, indeed, the  $\mathbf{E} \times \mathbf{B}$  drift velocity creates a ion flux pattern that keeps the divertor plasma rarefied and warm, driving it away from detachment. Specifically, the radial component of the  $\mathbf{E} \times \mathbf{B}$  velocity pushes ions from the CFR into the PFR, where the poloidal component of the  $\mathbf{E} \times \mathbf{B}$  velocity pushes the ions out of the slot towards the inner divertor [26,27]. The reduction of the radial electric field in SAS-V thus weakens such poloidal ion flow, diminishing the effect of drifts, densifying and further cooling the plasma in the slot.

Early modeling of the SAS-V divertor [13] explored a plasma density range where the SAS-V is always detached, i.e.  $T_{e,t} < 10 \text{ eV}$ . Here, we extend the modeling to lower plasma densities, to evaluate the effect of target shaping in attached conditions. At low density, where both SAS and SAS-V are attached, SOLPS finds that the

V-shape increases the outer divertor volumetric ionization and line radiation, figures 5a-b, but does not change the  $\mathbf{E} \times \mathbf{B}$  ion flux from the PFR towards the inner divertor, figure 5c. The drift flows are unaffected because the shape of the target electron temperature profile in SAS-V is similar to that in SAS, resulting in a similar temperature radial gradient, similar radial electric field and, thus, similar poloidal  $\mathbf{E} \times \mathbf{B}$  velocity. The  $\mathbf{E} \times \mathbf{B}$  ion flux from the PFR towards the inner divertor is  $\approx 50$  to  $80\%$  of the ion flux to the outer target. At higher density, where SAS-V is detached, the V-shape effect becomes twofold. In addition to the increased ionization and line radiation observed at low density, the V-shape also reduces the  $\mathbf{E} \times \mathbf{B}$  ion flux from the PFR towards the inner divertor, 5c, which further densifies and cools the plasma in the slot. This is the regime investigated in the previous modeling of SAS-V [13]. The drift flows are affected because the target temperature profile shape in SAS-V is flattened compared to SAS, leading to a substantial reduction of the radial electric field and thus of the poloidal  $\mathbf{E} \times \mathbf{B}$  velocity.

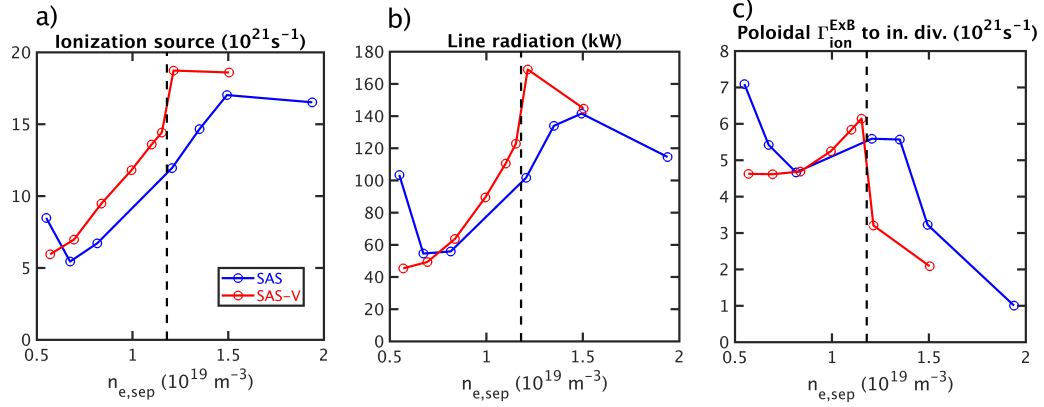


FIG. 5. For ion  $\mathbf{B} \times \nabla \mathbf{B}$  into the divertor, outer divertor (a) ionization source, (b) line radiation (deuterium and carbon) and (c) poloidal ion  $\mathbf{E} \times \mathbf{B}$  flux from outer to inner divertor (through the PFR), as a function of the separatrix electron density at the outboard mid-plane, for SAS (blue) and SAS-V (red). The dashed line indicates when the SAS-V divertor transitions to the detached regime. The poloidal ion  $\mathbf{E} \times \mathbf{B}$  flux through the PFR is localized between the separatrix and the  $\psi_n = 0.99$  flux surface.

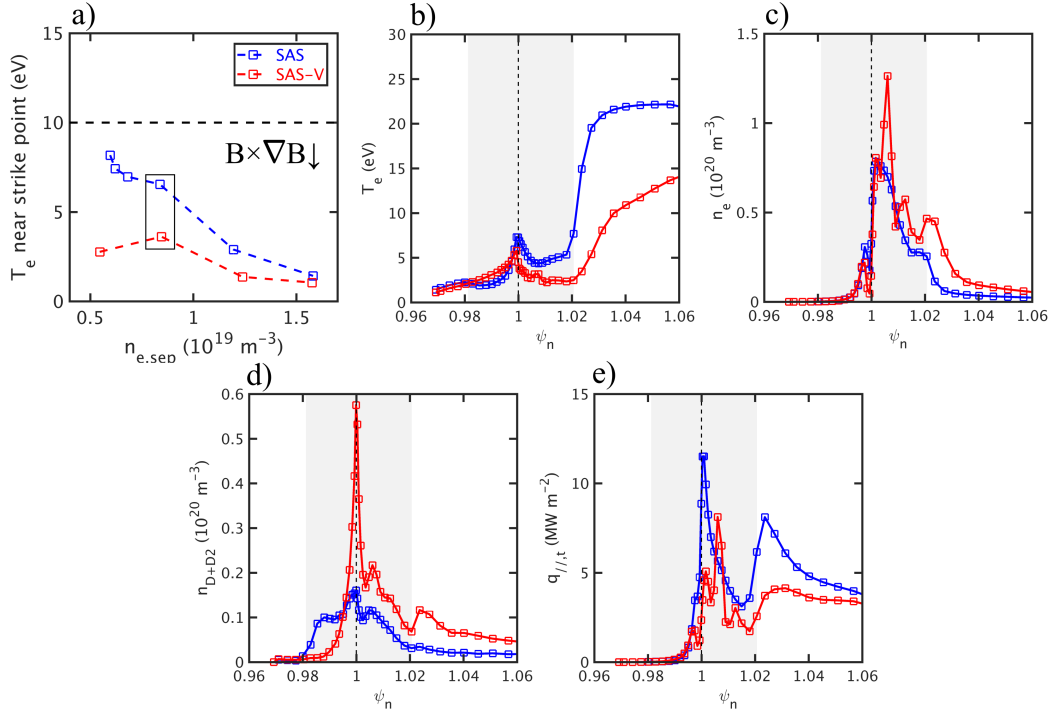


FIG. 6. For ion  $\mathbf{B} \times \nabla \mathbf{B}$  out of the divertor, (a) electron temperature near the strike point (third poloidal flux ring in CFR after separatrix) as a function of the separatrix electron density at the outboard mid-plane for SAS (blue) and SAS-V (red). For the same  $B_t$  direction, at the density  $n_{e,sep} = 0.84 \text{ } 10^{19} \text{ m}^{-3}$  indicated in sub-figure (a), target profiles of electron temperature (b), electron density (c), neutral density (d) and parallel heat flux (e), for SAS (blue) and SAS-V (red). The shaded area indicates the extent of the slot.

## B. Ion $\mathbf{B} \times \nabla \mathbf{B}$ drift out of divertor

For ion  $\mathbf{B} \times \nabla \mathbf{B}$  out of the divertor, SOLPS-ITER again finds that the electron temperature near the strike point is lower in SAS-V relative to SAS, for all simulated densities, figure 6a. The lower temperature correlates

with a higher neutral density, figure 6d. Modeling thus shows that the SAS-V divertor has an earlier onset of detachment relative to SAS for both  $B_t$  directions. Note that SOLPS finds only detached solutions for both SAS and SAS-V, and fails to converge at lower plasma densities, where attached plasma solutions are expected.

The effect of reversing the  $B_t$  direction is qualitatively similar in SAS and SAS-V. For ion  $\mathbf{B} \times \nabla\mathbf{B}$  out of the divertor, the  $\mathbf{E} \times \mathbf{B}$  drift pushes ions from the PFR across the separatrix into the CFR, increasing particle recycling from the outer small-angle slant, densifying and cooling the CFR plasma compared to the opposite  $B_t$  direction (compare figures 4b-c with 6b-c). The increased particle recycling is limited to the outer slant surface for SAS, whereas it extends out of the slot for SAS-V, causing a cooling also of the far-SOL, figure 6b, and a reduction of the heat load, figure 6e.

### C. Higher input power

The effect of the heating power on the performance of the SAS-V divertor is studied by increasing the input power from 4 MW to 8 MW, with ion  $\mathbf{B} \times \nabla\mathbf{B}$  drift into divertor, while keeping all other simulation inputs unchanged. SOLPS-ITER finds that the beneficial effect of the V-corner is reduced for increasing input power. At 4 MW, compared to SAS, SAS-V achieves  $T_{e,t} = 10$  eV with 11% lower upstream separatrix density, and  $T_{e,t} = 5$  eV with 16% lower upstream separatrix density. At 8 MW, however, the reduction of detachment thresholds is only 4% and 6% respectively, see figure 7.

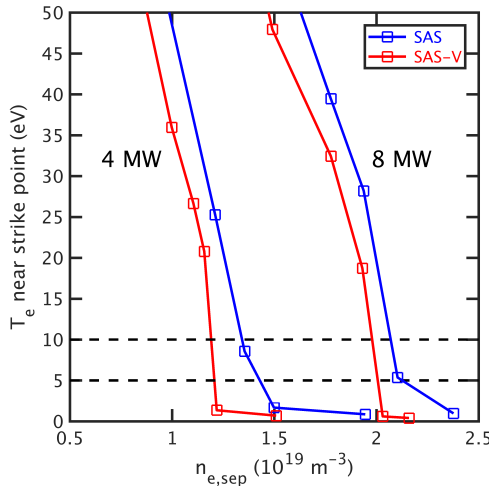


FIG. 7. For ion  $\mathbf{B} \times \nabla\mathbf{B}$  into the divertor, electron temperature near the strike point (third poloidal flux ring in CFR after separatrix) as a function of the separatrix electron density at the outboard mid-plane for SAS (blue) and SAS-V (red), with input power of 4 MW and 8 MW.

The dependence of the V-corner effect on heating power can be understood in terms of plasma collisionality. With higher input power, detachment onset ( $T_{e,t} = 10$  eV) is achieved at higher plasma density, figure 7, therefore higher plasma collisionality and lower ionization mean free path (m.f.p.). This means that recycled neutrals ionize, on average, at a shorter distance from the target and are, therefore, less sensitive to target shape

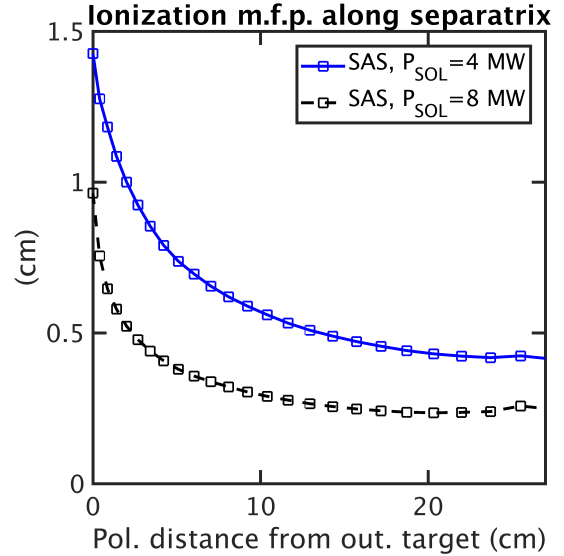


FIG. 8. For ion  $\mathbf{B} \times \nabla\mathbf{B}$  into the divertor, ionization mean free path along the separatrix in the SAS divertor, as a function of the poloidal distance from the target, for  $P_{\text{SOL}} = 4$  MW (blue) and 8 MW (black). The two simulations have similar electron temperature near the strike point ( $\approx 25$  eV), which is achieved by adjusting the outboard mid-plane separatrix electron density,  $n_{e,\text{sep}} = 1.21 10^{19} \text{ m}^{-3}$  for 4 MW and  $1.93 10^{19} \text{ m}^{-3}$  for 8 MW.

modifications. Analysis of the SOLPS output confirms that the ionization m.f.p. is  $\approx 30\%$  lower with  $P_{\text{SOL}} = 8$  MW compared to 4 MW, figure 8, for similar electron temperature near the strike point (achieved by adjusting the outboard mid-plane separatrix electron density).

The observed reduction of target shaping effectiveness with higher input power indicates that in a future fusion reactor, where the power crossing the separatrix will be high, divertor target shaping alone may be insufficient to mitigate target temperature and parallel heat fluxes below acceptable levels. Target shaping should be combined with additional strategies to lower the detachment density, such as in-slot puffing of low-Z impurities, which would in turn make the slot more effective.

### IV. SCAN OF STRIKE POINT POSITION

The performance of the SAS and SAS-V divertors is then evaluated by moving the strike point location in the slot at fixed plasma density ( $n_{e,\text{sep}} = 1.21 10^{19} \text{ m}^{-3}$  for ion  $\mathbf{B} \times \nabla\mathbf{B}$  into the divertor,  $1.19 10^{19} \text{ m}^{-3}$  for ion  $\mathbf{B} \times \nabla\mathbf{B}$  out of the divertor). The strike point sweep is built using the magnetic equilibria of DIII-D shot 176971 at different times. The optimal strike point position in the slot is defined as the one that most reduces both the near-SOL electron temperature and the peak parallel heat flux at the target.

### A. Strike point sweep in SAS

Good agreement between modeling and measurements is achieved for the strike point position scan in SAS, especially for the ion  $\mathbf{B} \times \nabla\mathbf{B}$  drift into the divertor. A detailed analysis of the plasma conditions for each strike point position is discussed in the following, and shown in figure 9.

For ion  $\mathbf{B} \times \nabla\mathbf{B}$  into the divertor (blue data points in figure 9), with the strike point on the inner slant (position A), SOLPS finds that the electron temperature is strongly reduced along the flat end, where neutral density is high, thus promoting volumetric dissipation and ionization. Electron temperature in the near-SOL and peak parallel heat flux are however high, because the near-SOL is on the inner slant, where neutral density is low. With the strike point on the flat end (positions B to D), the high neutral density maximizes volumetric dissipation and ionization, reducing the peak parallel heat flux by a factor 2. The electron temperature in the far-SOL increases because the far-SOL shifts to the outer slant, where neutral density is low. With the strike point at the outer corner, position D, the near-SOL temperature rises, in both modeling and experiment, such that the strike point re-attaches. This is the position used for the plasma density scan (Section III) and the early modeling of the SAS-V divertor [13]. Placing the strike point on the outer slant (position E) reduces the baffling of recycling neutrals from the inner and outer slants, and places the entire SOL in a region of low neutral density. This increases the electron temperature and the parallel heat flux.

For ion  $\mathbf{B} \times \nabla\mathbf{B}$  out of the divertor (black data points in figure 9), the effect of strike point sweeping is quite different than the opposite drift direction. Moving the strike point from the inner slant to the outer corner (positions A to D) causes a significant drop of electron temperature along the target and peak parallel heat flux. The temperature drop is clearly visible in both modeling and measurements. Moving the strike point closer to the outer corner, indeed, increases the particle recycling on the small-angle slant associated with the radial  $\mathbf{E} \times \mathbf{B}$  velocity, which pushes ions out of the PFR across the separatrix to the CFR. The increased recycling counteracts the reduced neutral baffling from the inner slant. Placing the strike point on the outer slant (position E) reduces the neutral baffling from both the CFR and PFR slants, which rarefies and warms the plasma, similarly to what is observed for the opposite drift direction.

SOLPS modeling and target measurement agree that the optimal strike point position is the inner corner for ion  $\mathbf{B} \times \nabla\mathbf{B}$  into the divertor, the outer corner for ion  $\mathbf{B} \times \nabla\mathbf{B}$  out of the divertor (sub-plots highlighted in yellow in figure 9).

### B. Strike point sweep in SAS-V

For ion  $\mathbf{B} \times \nabla\mathbf{B}$  into the divertor (blue data points in figure 10), SOLPS finds that moving the strike point along the outer slant towards the V-corner (locations A to D) shifts the near-SOL into the V-corner, where neutral density is maximal. This increases volumetric dissipation and ionization, lowering the electron temperature in the near-SOL, figure 10, and the peak parallel heat flux. The far-SOL temperature, in contrast, increases because the far-SOL shifts onto the outer slant, where neutral density is low. Placing the strike point on the outer slant (position E) reduces the neutral baffling from both the CFR and PFR slants, increasing electron temperature and parallel heat flux, similarly to SAS.

For ion  $\mathbf{B} \times \nabla\mathbf{B}$  out of the divertor (black data points in figure 9), moving the strike point from the outer slant towards the V-corner causes a significant decrease of electron temperature along the entire SOL and strongly reduces the peak parallel heat flux. Placing the strike point on the outer slant (position E) reduces the neutral baffling from both the CFR and PFR slants, increasing electron temperature and parallel heat flux.

SOLPS finds that the optimal strike point position is the V-corner for both  $B_t$  directions, in contrast to SAS, where it changes with the magnetic field direction.

## V. SUMMARY AND CONCLUSION

This paper presents extensive SOLPS-ITER modeling of DIII-D small-angle slot (SAS) divertor and of its upcoming upgrade, the V-shape small-angle slot (SAS-V) divertor. The modeling includes the effect of particle drifts, improving the fidelity over the approximations adopted in the first SAS-V simulations [13]. The objectives are to assess the performance of the SAS-V concept relative to SAS and, in parallel, to investigate the impact of divertor closure modifications on particle drift flows and onset of divertor detachment. Simulations are performed for a range of values of plasma density, heating power, strike point position in the slot and for both magnetic field directions. To increase the modeling accuracy, the cross-field anomalous transport coefficients prescribed in SOLPS are computed from experimental measurements.

SOLPS-ITER finds that the electron temperature near the strike point is reduced in SAS-V compared to SAS, for all simulated densities, heating powers and for both magnetic field directions. This means that the SAS-V divertor achieves detachment at a lower value of the upstream separatrix electron density compared to SAS. The lower detachment threshold is explained in terms of the V-corner ability to focus recycled neutrals, which densify and cool the plasma in the slot [13]. At sufficiently high density, and ion  $\mathbf{B} \times \nabla\mathbf{B}$  into the divertor, the V-shape thereby reduces the radial gradient of the electron temperature at the target, which in turn reduces the radial

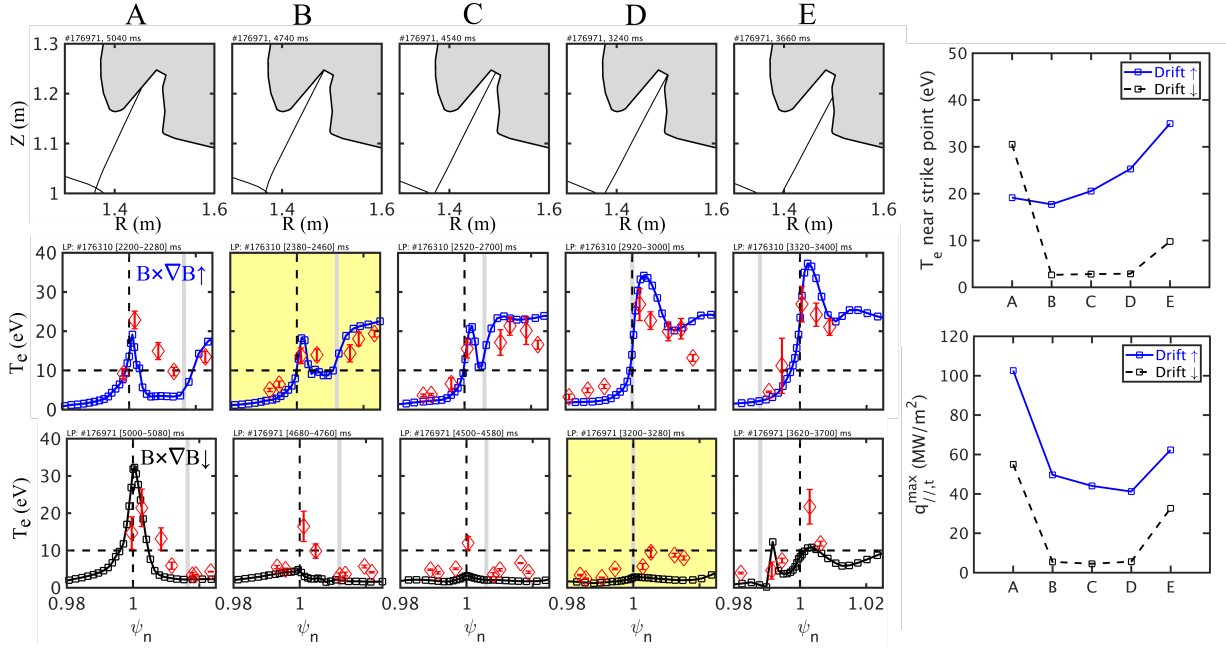


FIG. 9. (Left) Electron temperature profile in the SAS divertor for different strike point position (inner slant (A), inner corner (B), flat end (C), outer corner (D) and outer slant (E)), for  $\mathbf{B} \times \nabla \mathbf{B}$  into (blue) and out of (black) the divertor. Red diamonds correspond to Langmuir Probe measurements. Vertical gray lines correspond to the position of the flat end outer corner. (Right) Electron temperature near the strike point (top plot) and peak parallel heat flux (bottom plot) as a function of the strike point position, for  $\mathbf{B} \times \nabla \mathbf{B}$  into (blue) and out of (black) the divertor.

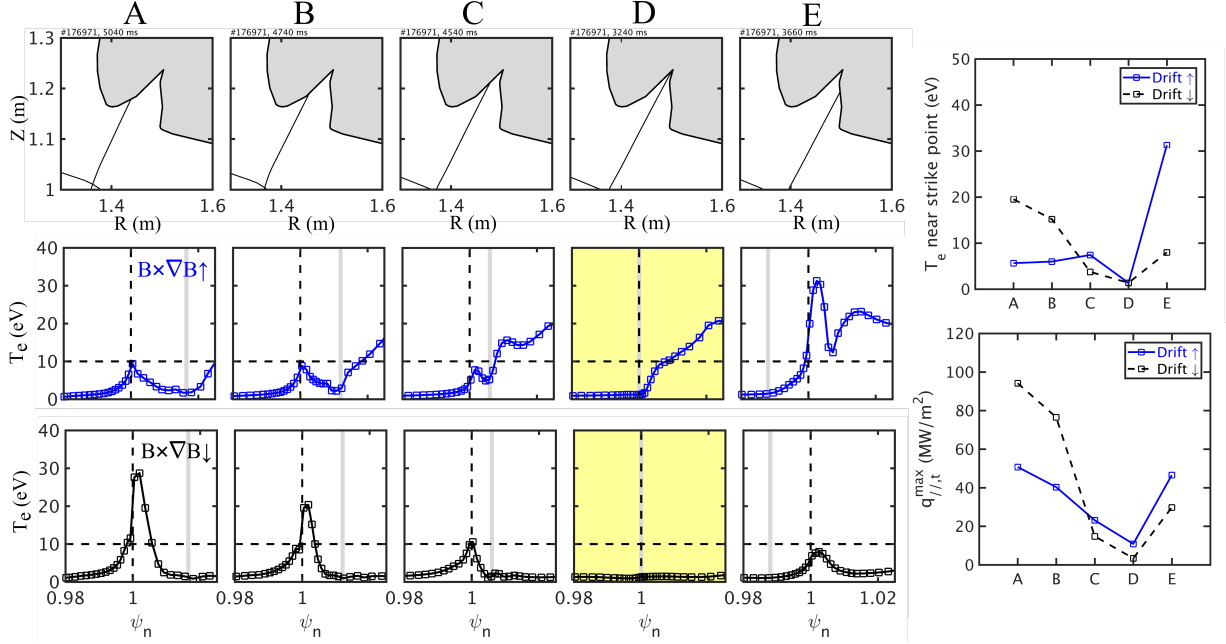


FIG. 10. (Left) Electron temperature profile in the SAS-V divertor for different strike point position (inner slant (A-B-C), V corner (D) and outer slant (E)), for  $\mathbf{B} \times \nabla \mathbf{B}$  into (blue) and out of (black) the divertor. Vertical gray lines correspond to the position of the V-corner. (Right) Electron temperature near the strike point (top plot) and peak parallel heat flux (bottom plot) as a function of the strike point position, for  $\mathbf{B} \times \nabla \mathbf{B}$  into (blue) and out of (black) the divertor.

electric field and thus the ion poloidal  $\mathbf{E} \times \mathbf{B}$  velocity, further densifying and cooling the plasma in the slot.

Modeling also finds that the V-shape effect on detach-

ment onset is less strong at higher input power. With more power crossing the separatrix, divertor detachment is achieved at a higher plasma density, thus higher plasma

collisionality and shorter ionization mean free path. Recycled neutrals ionize at a shorter distance from the target and thus are less sensitive to target shape modifications. Target shaping is, thus, less effective at higher input power, which suggests that in a fusion reactor, where heating power is high, target shaping needs to be combined with additional strategies to lower the detachment density, such as in-slot puffing of low-Z impurities, which would in turn make the slot more effective.

Finally, good agreement between modeling and experiment is achieved for the strike point position scan in SAS, showing that the optimal strike point position, where both electron temperature and peak parallel heat flux are minimal, is the slot inner/outer corner for ion  $\mathbf{B} \times \nabla \mathbf{B}$  into/out of the divertor, respectively. In SAS-V, modeling predicts that the optimal strike point position is the V-corner for both magnetic field directions, and that target plasma conditions change quickly if the strike point moves away from the V-corner.

To place the strike point on the V-corner and realize such optimal target conditions, the experiment will need, therefore, both a high degree of toroidal symmetry, achieved by carefully aligning the divertor tiles [28], and a high precision strike point control system, recently developed for SAS [29].

These results provide a useful reference for the upcoming DIII-D experimental campaign with the SAS-V divertor, and highlight key divertor design parameters for the design and operation of a new upper divertor. Future work will expand this analysis to high power seeded scenarios, featuring injection of deuterium atoms and low-Z impurities inside the slot, to assess the V-shape impact on impurity leakage from the slot.

## ACKNOWLEDGMENTS

The authors would like to thank the entire DIII-D Divertor Science and Innovation team, X. Bonnin, J. Guterl, A. E. Jaervinen, J. D. Lore and E. T. Meier for their help and constructive discussions. This material is based upon work supported by the U.S. Department of Energy, Office of Science, Office of Fusion Energy Sciences, using the DIII-D National Fusion Facility, a DOE Office of Science user facility, under Award(s) DE-FC02-04ER54698 and DE-AC05-00OR22725.

## DISCLAIMER

This report was prepared as an account of work sponsored by an agency of the United States Government. Neither the United States Government nor any agency thereof, nor any of their employees, makes any warranty, express or implied, or assumes any legal liability or responsibility for the accuracy, completeness, or usefulness of any information, apparatus, product, or process disclosed, or represents that its use would not infringe privately owned rights. Reference herein to any specific commercial product, process, or service by trade name,

trademark, manufacturer, or otherwise does not necessarily constitute or imply its endorsement, recommendation, or favoring by the United States Government or any agency thereof. The views and opinions of authors expressed herein do not necessarily state or reflect those of the United States Government or any agency thereof.

## REFERENCES

- [1] P. C. Stangeby *et al.*, "Basic physical processes and reduced models for plasma detachment," *Plasma Phys. Control. Fusion* **60** (2018), [doi.org/10.1088/1361-6587/aaacf6](https://doi.org/10.1088/1361-6587/aaacf6).
- [2] A. S. Kukushkin *et al.*, "Finalizing the ITER divertor design: The key role of SOLPS modeling," *Fusion Engineering and Design* **86**, 2865–2873 (2011), [doi.org/10.1016/j.fusengdes.2011.06.009](https://doi.org/10.1016/j.fusengdes.2011.06.009).
- [3] A. Loarte, "Effects of divertor geometry on tokamak plasmas," *Plasma Phys. Control. Fusion* **43**, R183–R224 (2001), [doi.org/10.1088/0741-3335/43/6/201](https://doi.org/10.1088/0741-3335/43/6/201).
- [4] A. Leonard, "Plasma detachment in divertor tokamaks," *Plasma Phys. Control. Fusion* **60**, 044001 (2018), [doi.org/10.1088/1361-6587/aaa7a9](https://doi.org/10.1088/1361-6587/aaa7a9).
- [5] J. T. (prepared by R.D. Monk), "Recent results from divertor and scrape-off layer studies at JET," *Nucl. Fusion* **39**, 1751 (1999), [doi.org/10.1088/0029-5515/39/11Y/315](https://doi.org/10.1088/0029-5515/39/11Y/315).
- [6] A. Kallenbach *et al.*, "Scrape-off layer radiation and heat load to the ASDEX upgrade LYRA divertor," *Nucl. Fusion* **39**, 901–917 (1999), [doi.org/10.1088/0029-5515/39/7/307](https://doi.org/10.1088/0029-5515/39/7/307).
- [7] N. Asakura *et al.*, "Role of divertor geometry on detachment and core plasma performance in JT60U," *Journal of Nuclear Materials* **266–269**, 182–188 (1999), [doi.org/10.1016/S0022-3115\(98\)00818-6](https://doi.org/10.1016/S0022-3115(98)00818-6).
- [8] B. Lipschultz *et al.*, "Divertor physics research on Alcator C-Mod," *Fusion Science and Technology* **51**, 369–389 (2007), [doi.org/10.13182/FST07-A1428](https://doi.org/10.13182/FST07-A1428).
- [9] A. Jaervinen *et al.*, "Interpretations of the impact of cross-field drifts on divertor flows in DIII-D with UEDGE," *Nuclear Materials and Energy* **12**, 1136–1140 (2017), [doi.org/10.1016/j.nme.2016.11.014](https://doi.org/10.1016/j.nme.2016.11.014).
- [10] A. Jaervinen *et al.*, " $E \times B$  flux driven detachment bifurcation in the DIII-D tokamak," *Physical Review Letters* **121**, 075001 (2018), [doi.org/10.1103/PhysRevLett.121.075001](https://doi.org/10.1103/PhysRevLett.121.075001).
- [11] H. Y. Guo *et al.*, "First experimental tests of a new small angle slot divertor on DIII-D," *Nucl. Fusion* **59** (2019), [doi.org/10.1088/1741-4326/ab26ee](https://doi.org/10.1088/1741-4326/ab26ee).
- [12] H. Y. Guo *et al.*, "Small angle slot divertor concept for long pulse advanced tokamaks," *Nucl. Fusion* **57** (2017), [doi.org/10.1088/1741-4326/aa5b46](https://doi.org/10.1088/1741-4326/aa5b46).
- [13] H. Du *et al.*, "Manipulation of ExB drifts in a slot divertor with advanced shaping to optimize detachment," *Nucl. Fusion* **60** (2020), [doi.org/10.1088/1741-4326/abb53f](https://doi.org/10.1088/1741-4326/abb53f).
- [14] X. Bonnin *et al.*, "Presentation of the new SOLPS-ITER code package for tokamak plasma edge modelling," *Plasma and Fusion Research* **11** (2016), [doi.org/10.1585/pfr.11.1403102](https://doi.org/10.1585/pfr.11.1403102).
- [15] R. Schneider *et al.*, "Plasma edge physics with B2-EIRENE," *Contrib. Plasma Phys.* **46**, 3–191 (2006), [doi.org/10.1002/ctpp.200610001](https://doi.org/10.1002/ctpp.200610001).
- [16] D. Reiter *et al.*, "The EIRENE and B2-EIRENE codes," *Fusion Science and Technology* **47**, 172–186 (2005), [doi.org/10.13182/FST47-172](https://doi.org/10.13182/FST47-172).
- [17] L. Lao *et al.*, "Reconstruction of current profile parameters and plasma shapes in tokamaks," *Nucl. Fusion* **25** (1985), [doi.org/10.1088/0029-5515/25/11/007](https://doi.org/10.1088/0029-5515/25/11/007).
- [18] E. Meier *et al.*, "Modeling  $E \times B$  drift transport in conceptual slot divertor configurations," *Contribution to Plasma Physics* **60**, e201900151 (2020), [doi.org/10.1002/ctpp.201900151](https://doi.org/10.1002/ctpp.201900151).

- [19] J. Roth *et al.*, “Analytic description of the chemical erosion of graphite by hydrogen ions,” Nucl. Fusion **36** (1996), doi.org/10.1088/0029-5515/36/12/I05.
- [20] J. M. Canik *et al.*, “Measurements and 2-D modeling of recycling and edge transport in discharges with lithium-coated PFCs in NSTX,” Journal of Nuclear Materials **415**, S409–S412 (2011), doi.org/10.1016/j.jnucmat.2010.11.084.
- [21] G. Haas *et al.*, “In vessel pressure measurement in nuclear fusion experiments with asdex gauges,” Vacuum **51**, 39–46 (1998), doi.org/10.1016/S0042-207X(98)00131-6.
- [22] M. W. Shafer *et al.*, “Dependence of neutral pressure on detachment in the small angle slot divertor at DIII-D,” Nucl. Materials and Energy **19**, 487–492 (2019), doi.org/10.1016/j.nme.2019.04.003.
- [23] S. L. Allen *et al.*, “Recycling and neutral transport in the DIII-D tokamak,” Journal of Nuclear Materials **162-164**, 80–92 (1989), doi.org/10.1016/0022-3115(89)90259-6.
- [24] M. Groth *et al.*, “Impact of carbon and tungsten as divertor materials on the scrape-off layer conditions in JET,” Nucl. Fusion **53**, 093016 (2013), doi.org/10.1088/0029-5515/53/9/093016.
- [25] M. Groth *et al.*, “Testing the role of molecular physics in dissipative divertor operations through helium plasmas at DIII-D,” Physics of Plasmas **24**, 056116 (2017), doi.org/10.1063/1.4982057.
- [26] A. Chankin *et al.*, “Influence of the  $E \times B$  drift in high recycling divertors on target asymmetries,” Plasma Phys. Control. Fusion **57**, 095002 (2015), doi.org/10.1088/0741-3335/57/9/095002.
- [27] X. Ma *et al.*, “First evidence of dominant influence of  $E \times B$  drifts on plasma cooling in an advanced slot divertor for tokamak power exhaust,” Nucl. Fusion **61**, 054002 (2021), doi.org/10.1088/1741-4326/abde75.
- [28] J. Watkins *et al.*, “Langmuir probe array for the small angle slot divertor in DIII-D,” Review of Scientific Instruments **92**, 053523 (2021), doi.org/10.1063/5.0043870.
- [29] D. Eldon *et al.*, “High precision strike point control to support experiments in the DIII-D small angle slot divertor,” Fusion Engineering and Design **160**, 111797 (2020), doi.org/10.1016/j.fusengdes.2020.111797.